Tailoring Mechanical Properties and Shear Band Propagation in ZrCu Metallic Glass Nanolaminates Through Chemical Heterogeneities and Interface Density

Andrea Brognara,* Ankush Kashiwar, Chanwon Jung, Xukai Zhang, Ali Ahmadian, Nicolas Gauquelin, Johan Verbeeck, Philippe Djemia, Damien Faurie, Gerhard Dehm, Hosni Idrissi, James Paul Best,* and Matteo Ghidelli*

The design of high-performance structural thin films consistently seeks to achieve a delicate equilibrium by balancing outstanding mechanical properties like yield strength, ductility, and substrate adhesion, which are often mutually exclusive. Metallic glasses (MGs) with their amorphous structure have superior strength, but usually poor ductility with catastrophic failure induced by shear bands (SBs) formation. Herein, we introduce an innovative approach by synthesizing MGs characterized by large and tunable mechanical properties, pioneering a nanoengineering design based on the control of nanoscale chemical/structural heterogeneities. This is realized through a simplified model $Zr_{24}Cu_{76}/Zr_{61}Cu_{39}$, fully amorphous nanocomposite with controlled nanoscale periodicity (Λ, from 400 down to 5 nm), local chemistry, and glass–glass interfaces, while focusing in-depth on the SB nucleation/propagation processes. The nanolaminates enable a fine control of the mechanical properties, and an onset of crack formation/percolation ($>$1.9 and 3.3%, respectively) far above the monolithic counterparts. Moreover, we show that SB propagation induces large chemical intermixing, enabling a brittle-to-ductile transition when $\Lambda \leq 50$ nm, reaching remarkably large plastic deformation of 16% in compression and yield strength $\approx$2 GPa. Overall, the nanoengineered control of local heterogeneities leads to ultimate and tunable mechanical properties opening up a new approach for strong and ductile materials.

1. Introduction

Commonly used approaches for enhancing the strength of crystalline alloys often revolve around the introduction of imperfections within the crystalline structure, including secondary phases, grain or twin boundaries, as well as the incorporation of foreign atoms into solid solutions. These strengthening mechanisms mainly focus on the generation and propagation of dislocations, the typical carriers of plasticity. Specifically, coherent nanoscale precipitation[1] and transformation-induced plasticity[2] have demonstrated the potential to enhance both strength and ductility, while often being mutually exclusive. Metallic glasses (MGs), introduced in the 1960s,[3] do not possess slip systems and lattice dislocations, manifesting superior yield strength close to the theoretical atomic decohesion limit.[4,5] However, the plastic deformation of MGs at T_{room} is highly localized in shear bands (SBs) thus leading to MGs' catastrophic failure without any significant macroscopic ductility.[4]

A. Brognara, C. Jung, X. Zhang, A. Ahmadian, G. Dehm, J. P. Best, M. Ghidelli
Max-Planck-Institut für Eisenforschung GmbH
Max-Planck-Str. 1, 40237 Düsseldorf, Germany
E-mail: a.brognara@mpie.de; j.best@mpie.de; matteo.ghidelli@lspm.cnrs.fr

A. Kashiwar, H. Idrissi
Institute of Mechanics, Materials and Civil Engineering (iMMC)
IMAP
Université catholique de Louvain
B-1348 Louvain-la-Neuve, Belgium

A. Kashiwar, N. Gauquelin, J. Verbeeck, H. Idrissi
Department of Physics, Electron Microscopy for Materials Science (EMAT)
University of Antwerp
B-2020 Antwerp, Belgium

A. Ahmadian
Institute of Nanotechnology
Karlsruhe Institute of Technology
76344 Eggenstein-Leopoldshafen, Germany

P. Djemia, D. Faurie, M. Ghidelli
Laboratoire des Sciences des Procédés et des Matériaux (LSPM)
CNRS
Université Sorbonne Paris Nord
93430 Villetaneuse, France

Introducing local heterogeneities at the atomic level by tailoring atomic segregation and free volume opens up the control over MGs' mechanical properties by deflecting and deferring the propagation of SBs during deformation, thus enhancing ductility.[6–9] Similarly, the development of nanoglasses and cluster-assembled glassy films with high density of glass–glass interfaces and strong chemical fluctuations[10,11] leads to large hardness (up to 9 GPa) and homogenous plastic deformations up to ≈10% due to the nucleation of multiple SBs uniformly distributed within the material.[10]

Another mechanism occurs when MGs undergo homogeneous plastic flow in cases where their size is reduced below 500 nm (such as for thin-film MGs, TFMGs), triggering mechanical size effects mitigating SB nucleation/propagation while enhancing yield strength, ductility, and hardness.[4,12,13] This approach is often combined with the design of nanolayered architecture (few nm) benefiting from the interfaces and chemical effects providing suppression/mitigation of SB process within TFMGs.[14–20] Specifically, the introduction of crystalline nanolayers with different chemical/structural nature block SBs process, while the interfaces favor local intermixing phenomena resulting in a controlled and boosted mechanical behavior with large plasticity.[14,15,20] As an example, by alternating 16 nm thick nanocrystalline Cu layers and 112 nm thick $Cu_{50}Zr_{50}$ MGs, Kim et al.[14] obtained films with tensile strength and fracture strain respectively up to ≈2.5 GPa and ≈4%. Guo et al. instead deposited similar amorphous ZrCu/crystalline Cu nanolaminates (NLs) with a flow stress of 2.5 GPa and an exceptional 40% strain in compression, without fracture,[15] highlighting the potentially advantageous role of introducing further geometric constraint in TFMG systems.

Studies on fully amorphous NLs also highlight the potential of amorphous–amorphous interfaces and heterogeneities in mitigating catastrophic SBs and improving the mechanical properties of TFMGs compared to monolithic and largely chemically homogeneous TFMGs.[16–18] Chen et al.[16] explored the relationship between hardness of NiNb/ZrCuNiAl NLs' bilayer period (Λ), and interfaces morphology. A maximum hardness equal to 8.4 GPa was found for $\Lambda = 50$ nm, exceeding the value of the hardest single component, i.e. 8 GPa of ZrCuNiAl. Kuan et al.[17] suggested that alternating amorphous layers with different elastic moduli can mitigate the brittleness of TFMGs by obstructing SBs propagation during micropillar compression. Sharma et al.[18] carried out compression tests of micropillars of amorphous Zr-based/La-based NLs reporting larger plasticity compared to the monolithic references. The authors suggested that the softer La-based layers act as preferential nucleation site for SBs which, however, were unable to propagate into the higher critical shear-stress Zr-based layers. Therefore, SBs remain confined and multiply within the soft layers, accommodating the plastic deformation. Kontis et al.[21] fabricated $CoTaB_x$ TFMGs with a self-assembled lamellar structure as result of local chemical segregation, affecting fracture toughness and hardness. Finally, recently Wu et al.[22] produced Ti–Zr–Nb–Si- and Mg–Zn–Ca-based hierarchically nanodomained amorphous alloy with nanoscale interfaces, influencing chemical intermixing during SB propagation and increasing plasticity micropillar compression up to 40%.

However, the development of fully amorphous NLs, benefiting from their intrinsically superior yield strength, is still missing especially when the intrinsic size is below 10 nm, namely equal to or below the typical size of a SB event.[23] In addition, a thorough analysis of the mechanical behavior as well as of the nucleation/propagation of SBs and their interactions in such fully amorphous architectures with a tailored interface density (bilayer period from 200 down to 5 nm) has never been tackled, requiring the need of multiscale characterization techniques from the micrometer down to the atomic scale.

Here, we designed and fabricated nanoscale periodic chemical heterogeneities constituted by ZrCu fully amorphous NLs with controlled bilayer period (Λ) from 400 down to 5 nm, while investigating the mechanical behavior through a set of advanced scale-bridging techniques. In parallel, we investigated the local chemical evolution during SBs process through advanced transmission electron microscopy (TEM) and atom probe tomography (APT). We show how the interfaces and chemical heterogeneities can influence the mechanical behavior of films and SB formation and propagation processes depending on Λ and the total film thicknesses, activating large mechanical size effects as well as a controlled brittle-to-ductile transition with large chemical intermixing within the nanolayers.

2. Results and Discussion

The fully amorphous nanocomposite with tunable nanoscale local heterogeneities and interfaces has been designed in a form of an "easy-to-fabricate" model involving a fine control of $Zr_{24}Cu_{76}$ and $Zr_{61}Cu_{39}$ sublayers, benefiting from the large glass-forming ability and the different local atomic order as reported in Figure S1, Supporting Information (SI). Moreover, these compositions have shown the largest mismatch of mechanical properties with elastic moduli and hardness values of 102 and 78 GPa, and 7.7 and 5.5 GPa, respectively,[24] thus, aiming to create effective barriers against the propagation of SBs and deformation.[17,18]

The introduction of heterogeneities has been carried out by varying the number of interfaces with different bilayer period (Λ) from 400 down to 5 nm to trigger mechanical size effects especially when approaching the characteristic size of SBs (≈10 nm).[23] Moreover, the effect of the total thickness (i.e., 400 nm and 3 μm) was explored to further enhance the thickness confinement and how it influences the SB process. **Table 1** reports the complete list of NLs investigated.

The investigation on NLs structure, local chemical fluctuations, and interfaces was performed with scanning transmission electron microscope (STEM). **Figure 1**a–c displays high-angle annular dark-field (HAADF)–STEM images of 400 nm thick NLs with Λ equal to 200, 50, 25, and 5 nm, respectively. $Zr_{24}Cu_{76}$ and $Zr_{61}Cu_{39}$ layers show bright and dark contrasts,

Table 1. Fully amorphous NLs fabricated in this work. The bottom and top compositions are, respectively, $Zr_{24}Cu_{76}$ and $Zr_{61}Cu_{39}$ (at.%).

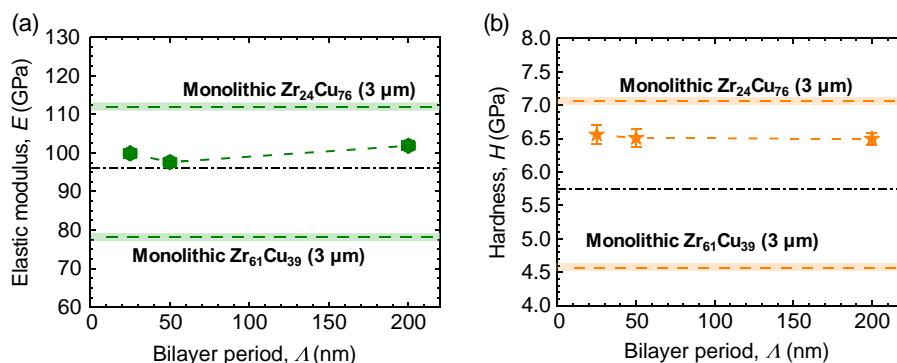|	Total thickness: 400 nm	Total thickness: 3 μm
Bilayer period (Λ)	400, 200, 100, 50, 40, 25, 10, 5 nm	200, 50, 25 nm
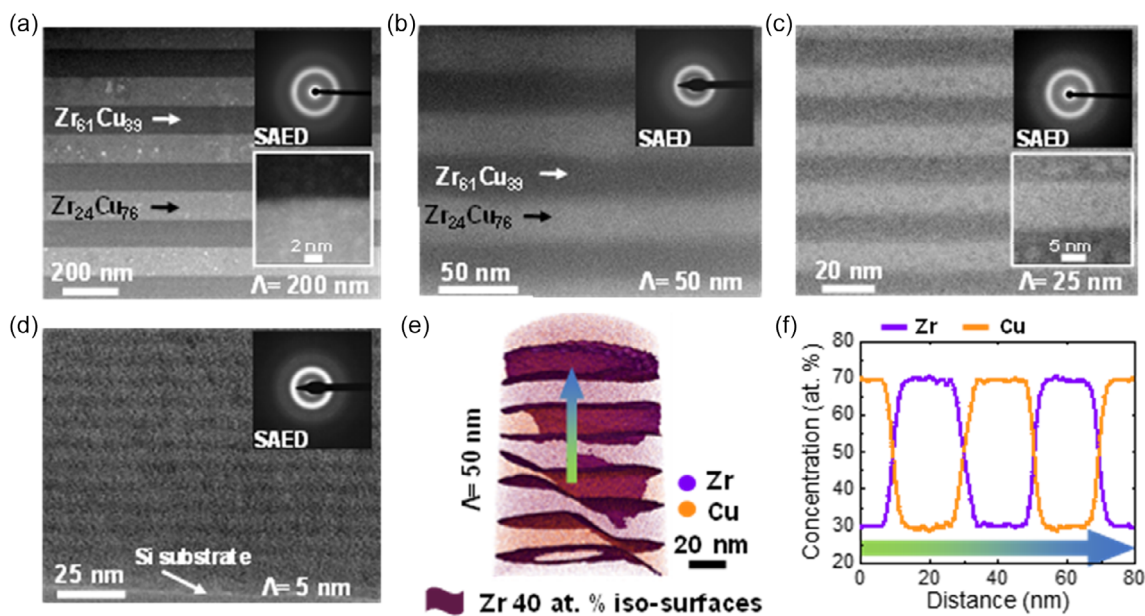
Figure 1. HAADF–STEM micrographs of a 3 µm thick NLs with Λ equal to a) 200, b) 50, and c) 25 nm and that of d) a 400 nm thick NL with Λ = 5 nm. The different layers can be distinguished with bright and dark contrast corresponding to $Zr_{24}Cu_{76}$ and to $Zr_{61}Cu_{39}$ (see the EELS analysis in Figure S3, Supporting Information, and the EDS map in Figure S4, Supporting Information), respectively. Insets of (a,c) show the presence of sharp and straight interfaces for Λ = 200 nm, while as Λ decreases, (b–d) the interfaces appear progressively less defined. SAED patterns are reported in the insets in (a–d) confirming that the films are fully amorphous. e) The 3D atom map acquired from APT analysis of a tip extracted from a 3 µm thick NL with Λ = 50 nm. f) The 1 d concentration profile in the direction of the color gradient arrow, corresponding to a cylindrical region of interest of Φ 20 × 80 nm^3.

respectively, as shown in the HAADF–STEM image and energy-dispersive X-ray spectroscopy (EDS) maps in Figure S2, SI. The Cu-rich layers exhibit brighter contrast due to their higher mass density compared to the Zr-rich layers (i.e., respectively 8.36 and 7.45 g cm^{-3}).[24] This is further confirmed from the electron energy loss spectroscopy (EELS) measurements (Figure S3, SI) that show higher relative thickness for Cu-rich layers than Zr-rich layers. The STEM micrographs clearly highlight the presence of a nanolayered architecture, even for Λ as less as 5 nm (see Figure 1d). Insets in Figure 1a,c display higher resolution STEM images which show the presence of sharp interfaces for both Λ equal to 200 and 50 nm. Selected area electron diffraction (SAED) patterns in the insets of Figure 1a–d acquired in regions including both $Zr_{24}Cu_{76}$ and $Zr_{61}Cu_{39}$ layers indicate the presence of a fully amorphous structure with no evidence of crystallinity. Further information on the composition fluctuations and the chemistry at the interfaces was obtained from the APT measurement performed on the 3 µm thick NL with Λ = 50 nm. The APT tip was specifically extracted below a nanoindent to capture the results of SBs deformation, see discussion in Section 3.3. In Figure 1e, layer interfaces are highlighted by Zr 40 at.% iso-surfaces. From the chemical profile evolution (Figure 1f) extracted in the region not deformed by the SB and highlighted by the color gradient arrow in Figure 1e, a clear separation between the different layers is evident. The composition of the individual layers $Zr_{30}Cu_{70}$/$Zr_{70}Cu_{30}$ is slightly different but consistent with the nominal $Zr_{24}Cu_{76}$/$Zr_{61}Cu_{39}$ compositions of the monolithic films obtained by scanning electron microscopy (SEM)/EDS (Figure S4, SI), indicating that negligible intermixing occurred during synthesis resulting from the high accuracy of APT.

Based on the STEM images in Figure 1, as Λ decreases, the layers' interfaces progressively appear less sharply defined, especially for Λ = 5 nm (Figure 1d). A similar trend was also reported by Chen et al.[16] which described interfaces to be less defined and with a transition from straight to wavy when $\Lambda \leq 100$ nm. This was related with the presence of the large intermixing between layers during the deposition process, which was higher for NLs with moderate layer thicknesses (i.e., $\Lambda \leq 100$ nm), as also shown, for instance, for Ni/Ti NLs $\Lambda \leq 30$ nm.[25]

Figure 2 reports the nanoindentation results of the 3 µm thick films as a function of Λ. The values of elastic modulus (E) for thick NLs (Figure 2a) appear to be rather constant for the different Λ equal to 200, 50, and 25 nm and lie only slightly above the rule of mixture (ROM) of both components (i.e., $Zr_{24}Cu_{76}$ and $Zr_{61}Cu_{39}$). Similarly, the values of hardness (H) are not dependent on Λ, but are $\approx$1 GPa above the ROM and closer to the harder Cu-rich layer, suggesting that the presence of heterogeneities and interfaces has an impact on the NLs' plastic deformability.

To better understand the interaction between chemical heterogeneities, interfaces, and deformation, STEM and APT measurements were performed on the regions under two residual nanoindentation imprints of a 3 µm thick NL with Λ = 50 nm (**Figure 3**). The STEM micrograph in Figure 3a shows the deformation and SBs propagation through the $Zr_{24}Cu_{76}$ and $Zr_{61}Cu_{39}$ layers (white arrows). The propagation of SBs induces both deformation of the individual layers and a misalignment of the original layers stack. Nevertheless, after the initial propagation, the SBs are arrested in Cu-rich layers, green arrows in Figure 3a. As a matter of fact, $Zr_{24}Cu_{76}$ layers have higher shear

**ADVANCED
SCIENCE NEWS**

www.advancedsciencenews.com

**small
structures**

www.small-structures.com

Figure 2. Comparison between a) elastic modulus (E) and b) hardness (H) values from CSM nanoindentation for 3 μm thick NLs as a function of bilayer period (Λ). The values of E remain close to the rule of mixture (ROM) (i.e., black dash-dot lines), while the values of H are higher and close to those of the harder $Zr_{24}Cu_{76}$. The dashed lines in the graphs represent the values for monolithic reference films ($Zr_{24}Cu_{76}$ and $Zr_{61}Cu_{39}$) and the shadowed regions represent the respective error bars.
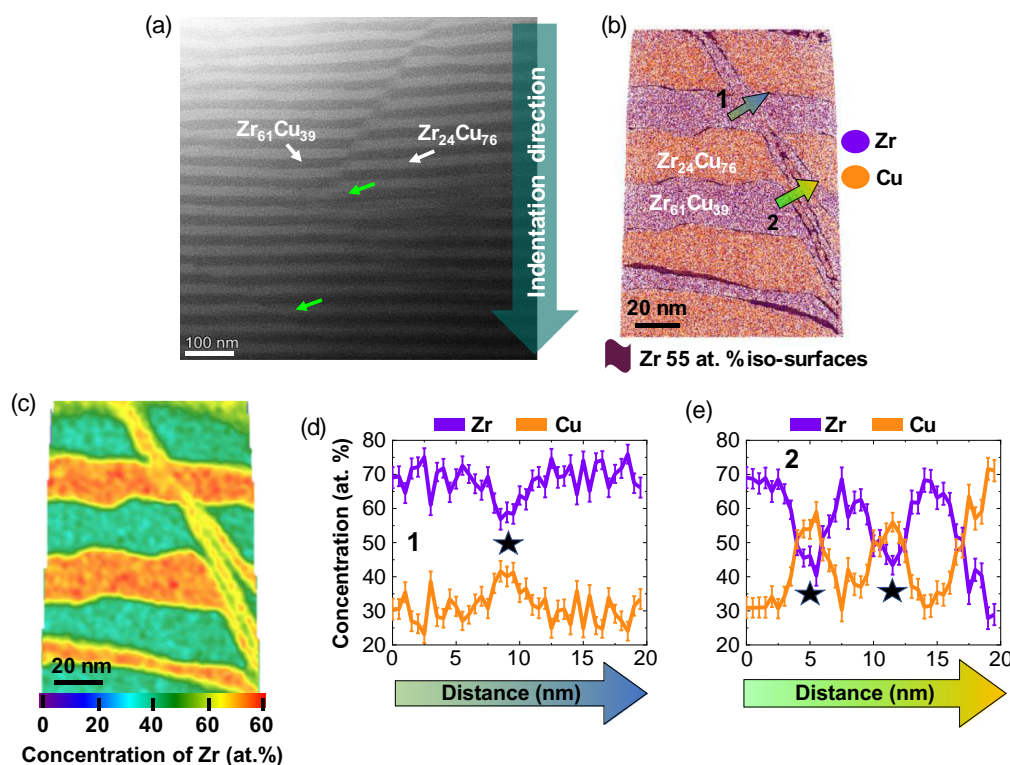
Figure 3. Chemical evolution along shear banding process underneath a nanoindent on a 3 μm thick NL with $\Lambda = 50$ nm. a) The HAADF–STEM image shows the propagation of the SB which stops at the stiffer Zr24Cu76 layers (green arrows), acting as deformation barriers. b) APT sample highlighting the severe deformation along SB events causing a mismatch of the original layer stack (5 nm thin slice viewed along the × axis, extracted from Figure 1e). c) The 2D contour plot of Zr (identical region with (b)) and d,e) 1D concentration profiles (i.e., within cylindrical regions of interest of Φ4 × 20 nm) of two different points across the SB path indicated by (1) and (2) gradients in (b) highlighting the large chemical intermixing between the layers.

resistance[26] and exhibit more significant obstacle toward SBs propagation due to the presence of strong Cu—Cu bonds and the higher content of full-icosahedral clusters with respect to $Zr_{61}Cu_{39}$ layers.[24]

APT measurement was also able to capture the deformation process, providing more in-depth information on the chemical evolution induced by the interaction between SBs and the

heterogeneous NLs structure (Figure 3b–e). The SB has a characteristic width of ≈ 10 nm, in agreement with literature on ZrCu,[23] while its propagation induces a mismatch in the original layer stack. Moreover, the SB propagates through the layers, resulting in severe local deformation following the indentation loading direction. However, although the layers are misaligned, they are not dissolved by the SB. Indeed the two sides (i.e., left

and right) remain connected by a thinner portion, indicating the ability of the NL to sustain plasticity through the deformation of its individual layers. The 2D contour plot of Zr (Figure 3c) and the 1D concentration profiles carried out across the SB path (i.e., Figure 3d,e, respectively, by the 1) green–blue and 2) green–yellow gradient arrows in Figure 3b) highlights the deformation-induced chemical intermixing between the layers. Indeed, the regions marked by the stars in Figure 3d,e have chemical concentration values in between those of the Zr- and Cu-rich layers, indicating the presence of localized chemical intermixing.

To the best of our knowledge, our work explored for the first time the chemical intermixing phenomena occurring in fully amorphous heterostructures providing further insights on the effects of SBs propagation, while highlighting the role of both morphological deformations (i.e., layers strain) and rearrangement of the local chemistry. Moreover, atomic intermixing phenomena is also promoted by elementary defects responsible of plasticity in both crystalline[27,28] and amorphous materials.[22] For the first case, it is observed that highly deformed crystalline alloys dislocations drag highly concentrated atoms from one phase to another, inducing composition homogenization of the alloy during plastic deformation.[27,28] In MGs, the plasticity carriers are shear transformation zones (STZs), >600 atoms (few nm^3),[29] whose activation/percolation is responsible of the SB process. The activation of STZs induces appreciable rearrangement of atoms between the adjacent amorphous nanodomains facilitating homogenization, rather than phase separation toward equilibrium reported inside some SBs.[30] Moreover, such phenomena can also be boosted by the severe local heating effects caused by SBs propagation, which can induce local temperature increments even exceeding the melting temperature.[31–33] Finally, the large intermixing, the alternation of layers with different atomic structure,[26] and the presence of interfaces hinders the propagation of SBs explaining the larger H compared with the ROM.
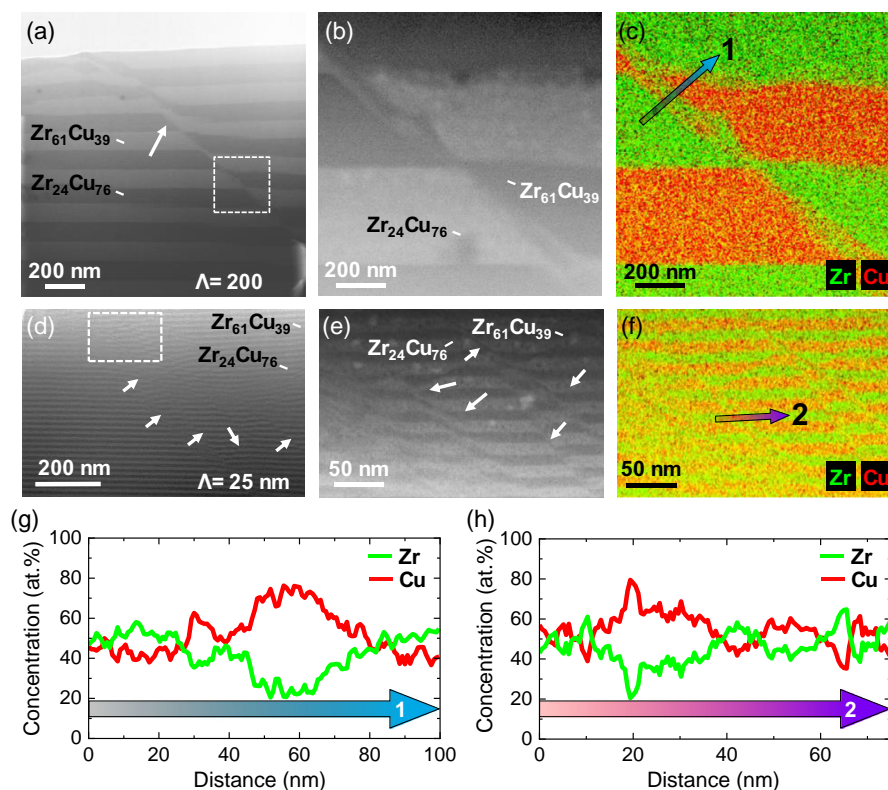
Micropillar compression was used to investigate the behavior of fully amorphous NLs in a different loading condition (i.e., uniaxial deformation) compared to nanoindentation and to investigate the role of periodical heterogeneities on the plasticity.

Figure 4a reports the compression tests of different NLs compared with the monolithic $Zr_{24}Cu_{76}$ and $Zr_{61}Cu_{39}$ counterparts. The monolithic films deform with formation of single catastrophic SBs characteristic of MGs,[34,35] corresponding to the sudden strain bursts in the load curve (experiments are carried out in force control). The yield stress (σ_y) before formation of SBs (Figure 4b) is dependent on film composition, with $Zr_{24}Cu_{76}$ showing an average σ_y of $2.30 \pm 0.09\,GPa$, well above the $1.70 \pm 0.07\,GPa$ of $Zr_{61}Cu_{39}$. This is due to the different local atomic order and packing on film composition with Cu-rich compositions characterized by a larger content of full icosahedral atomic clusters with high resistance against shear deformation.[24,26,36]

The NLs that have large σ_y in between 1.5 ± 0.65 and $1.8 \pm 0.22\,GPa$ close to the monolithic $Zr_{61}Cu_{39}$ (Figure 4g) are affected by the presence of the softer Zr-rich layers (having lower critical shear stress[26]) as well as by the presence of interfaces favoring the nucleation of SBs which are originated at free volume-rich interfaces.[10,37,38] For $\Lambda = 200\,nm$, NLs behave as the monolithic films, undergoing an abrupt brittle failure (i.e., yellow curve in Figure 4a). For $\Lambda = 200\,nm$ NLs behave as the monolithic films, undergoing an abrupt brittle failure (i.e., yellow curve in Figure 4a). However, for $\Lambda \leq 50\,nm$, the compression curves show a completely different behavior with small strain bursts and a very large plasticity, with no catastrophic failure up to strain values of $\approx 15\%$ (the load drops to zero for $\Lambda = 50$ and 25 nm are not due to SBs but correspond to the two unloading cycles performed during the tests). Therefore, the larger number of interfaces could effectively hinder the propagation of SBs as a result of the presence of the more shear-resistant Cu-rich layers, which, as reported in the TEM analysis on nanoindents, are able to act as barrier against SBs as was also shown in Ref. [24]. The presence of discrete stress increments in the stress–strain curves for the NLs with $\Lambda = 25$ and 50 nm in Figure 4a can be explained by our observation that large secondary shear events propagate through a previously locally deformed volume of material, originating from delocalized plasticity at interfaces, and higher stresses are required for propagation.
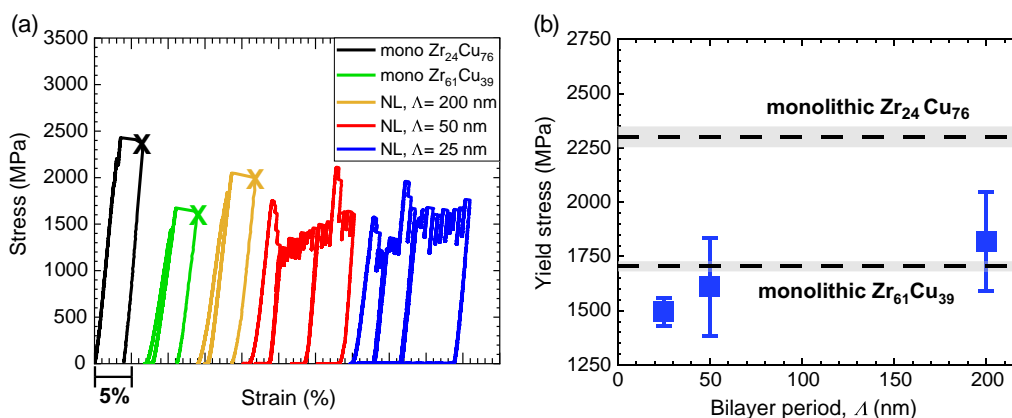
Figure 4. a) Selection of micropillar compression curves for 3 μm thick monolithic films and NLs (the rest of the curves are reported in Figure S6, Supporting Information). The curves have been shifted horizontally to facilitate data visualization. Monolithic films and NLs with $\Lambda = 200\,nm$ fail with formation of large SB events which cause strain bursts and load drops to zero; for NL with $\Lambda = 50$ and 25 nm, SBs propagation is suppressed while reporting a large apparent plasticity (the load drops are due to the two unloading cycles performed during the tests). b) Evolution of the yield stress (σ_y).

**ADVANCED
SCIENCE NEWS**

www.advancedsciencenews.com

**small
structures**

www.small-structures.com

Figure 5. Postmortem TEM analysis on NL pillars. a) Bright-field STEM (BF-STEM) and b) higher-magnification HAADF–STEM image from the region shown in (a); c) EDS composition Zr–Cu map of a compressed pillar with $\Lambda = 200$ nm showing the formation of a single SB. d) BF-STEM and e) higher-magnification HAADF–STEM from the region shown in (d); f) EDS map of a compressed pillar with $\Lambda = 25$ nm reporting a large number of SBs (white arrows). g,h) The EDS line scan for NL with $\Lambda = 200$ and 50 nm, respectively, acquired in the color gradient arrows 1 and 2 in (c,f) (areas of 100×25 and 75×5 nm^2, respectively). (g,h) The large chemical intermixing induced by SB propagation.

Figure 5a shows the post-mortem STEM analysis performed on the NL pillars with Λ of 200 and 25 nm. NLs with $\Lambda = 200$ nm deform with propagation of a single SB through the pillar, while for $\Lambda = 25$ nm multiple SBs are generated within the pillar volume (white arrows in Figure 5d,e). STEM and EDS analyses of pillars with $\Lambda = 200$ and 25 nm reveal that SBs induce not only mismatch in the layers stack, but also chemical intermixing between the layers. As for nanoindentation (Figure 3), it can be noticed that in spite of SBs propagation, in several regions (i.e., white arrows in Figure 5a,d,e), the layers resist the disruption and exhibit large plastic strain to accommodate the SBs propagation. In particular, for $\Lambda = 25$ nm, the SBs paths are also interrupted preventing their percolation (Figure 5e), as also suggested by the micropillar compression curves (Figure 4a). Figure 5c displays the EDS map for $\Lambda = 200$ nm with a line scan extracted on the zone severely deformed by the SB propagation (Figure 5g). The concentration profile shows that the portion of the $Zr_{24}Cu_{76}$ layer strained by the SB has a lower Cu at. % content than expected. Similarly, the EDS linear scan through a $Zr_{61}Cu_{39}$ layer of the NL with $\Lambda = 25$ nm (EDS map and concentration profile in Figure 5f,h) highlights that the composition is not constant and does not match with the nominal one. These results agree with the APT and nanoindentation data (Figure 3), highlighting that SB propagation induces layer intermixing, which can be observed for all the Λ studied (i.e., Figure 3–5).

The description of the mechanical behavior relies on the interplay of multiple effects that involve the presence of interfaces and structural–chemical heterogeneity. Softer Zr-rich layers are more prone to facilitate the nucleation of SBs whereas the Cu-rich layers and interfaces introduce the blocking effect. As reported by other studies on amorphous heterostructures,[10,37,38] despite interfaces act as potential barriers for SBs propagation, they can also nucleate SBs due to their lager free volume content. Therefore, the more frequent alternation of Zr-rich layers and interfaces for low Λ NLs can accommodate a larger number of SBs with more homogeneously distributed SB nucleation sites within the material volume. This prevents the formation of single catastrophic events and also justifies the gradual softening for NLs as Λ decreases (Figure 4b). However, the SB multiplication effect allows the low Λ NLs to exhibit a very large plastic deformation of $\approx$15% (while keeping a very high $\sigma_y = 1.5 \pm 0.65$ GPa), contrary to the NL with $\Lambda = 200$ nm and the monolithic films which suffer from the brittle failure. Finally, the presence of the Cu-rich layers with larger shear resistance are less easily penetrable for the SBs generated in the softer Zr-rich layers further promoting the homogeneous deformation and recovering plasticity[37,39,40] The combination of these mechanisms enable

the suppression of catastrophic failure of pillars and promote an exceptionally large plasticity when $\Lambda \leq 50$ nm.

The mechanical behavior of NL structures was investigated for films with total thickness of 400 nm as well, in order to achieve a larger confinement and to investigate its effect on the mechanical properties.[12,13] **Figure 6**a reports the evolution of E versus Λ by optoacoustic techniques, showing average values in between those of monolithic $Zr_{24}Cu_{76}$ and $Zr_{61}Cu_{39}$ references. However, a discrepancy is detected compared to the theoretical ROM value for an ideal NL with perfect interfaces (i.e., the

dash-dot black line in Figure 6a), with E values close to the ROM ($\Lambda = 400$ nm and <50 nm), while E increased toward monolithic $Zr_{24}Cu_{76}$ for $\Lambda = 50$ and 100 nm. This deviation can be related to the presence of defects at the interfaces such as higher free volume,[10,37,38] or variations of composition/density.[41] Indeed, the APT 1D concentration profile (Figure 1f) highlighted that the transition from one layer to the other is not perfectly sharp, suggesting the presence of a composition gradient at the interfaces between the layers, as well as of large layer compositional intermixing. Finally, for $\Lambda < 50$ nm, the elastic properties follow again the mixing rule (more distributed chemical variation).

Figure 6b,c reports the E and H values of 400 nm thick NLs obtained by continuous stiffness measurement (CSM) nanoindentation showing a strong dependence on Λ. As from optoacoustic measurements (Figure 6a), for $\Lambda = 400$ nm (i.e., only one interface), E and H have values very close to the ROM. However, as the number of interfaces increases (i.e., Λ decreases), E and H values progressively increase up to a maximum of, respectively, 152 and 12.5 GPa for $\Lambda = 50$ nm, well above that of the ROM and even higher than the monolithic references. To exclude any artifact due to CSM method, standard indentation measurements at different penetration depths were performed on the NL with $\Lambda = 50$ nm, but the results (Figure S5, Supporting Information) showed agreement between CSM and standard indentation. For $\Lambda < 50$ nm, E starts decreasing reaching ≈ 100 GPa when $\Lambda = 5$ nm. These results are clearly different from those with 3 µm thickness (Figure 2) which did not show a dependence E and H versus Λ. Moreover, although for 3 µm thick NLs E and H values were larger than the ROM, they remained lower than the values for the $Zr_{24}Cu_{76}$ monolithic reference. Differences in residual stresses can be excluded since they are generally very low and without a significant dependence of Λ or thickness (Table S1, Supporting Information).

The E and H values of the $Zr_{24}Cu_{76}$ monolithic references increase from ≈ 112 to ≈ 120 GPa and from ≈ 7 to ≈ 8 GPa for monolithic $Zr_{24}Cu_{76}$ when the film thickness decreases from 3 µm down to 400 nm. Similarly, for monolithic $Zr_{61}Cu_{39}$, E and H vary from ≈ 78 to ≈ 88 GPa and from ≈ 4.5 to ≈ 5.5 GPa, respectively. In discussing the present results, the presence and influence of the hard Si substrate must be considered. Indeed, due to the relatively thin thickness (i.e., 400 nm) of the films, it is expected that substrate effects can lead to an increase in the values of E and H measured by nanoindentation, compared to those obtained for 3 µm films. However, it is also known that at low thicknesses (i.e., <500 nm), TFMGs can show the activation of extrinsic size effects, dealing with thickness and substrate confinement, interfering with the formation of SBs for the thinner specimens.[4,12] This is also supported by the raw CSM nanoindentation curves (Figure S5, SI), showing that E and H values are higher for the 400 nm thick NLs and of the monolitic constituents independently on the penetration depth. Even though the higher values of E and H exhibited by the 400 nm thick NLs compared to their 3 µm counterparts is due to contributions from the substrate, the role of interfaces cannot be neglected (Figure 6b,c). Indeed, the E and H of the 400 nm NLs exhibit a clear dependency from Λ and the presence of interfaces, reaching values higher than the monolithic films with the same thickness (i.e., for 25 nm $\leq \Lambda \leq$ 100 nm). Therefore, the
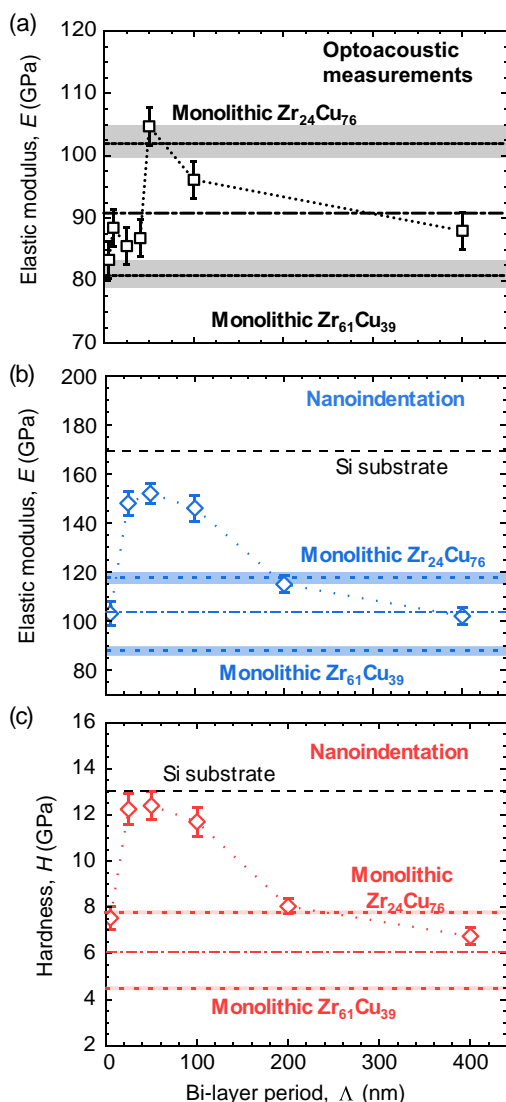
Figure 6. Elastic modulus (E) and hardness (H) of 400 nm thick NLs. a) The evolution of NLs' E versus Λ by optoacoustic techniques showing the of effect interfaces as a deviation from the ROM. b,c) Nanoindentation measurements reporting a string variation of E and H from the ROM values up to a maximum for $\Lambda = 50$ nm of 152 and 12.5 GPa for E and H, respectively. The dashed lines represent the values for monolithic reference films ($Zr_{24}Cu_{76}$ and $Zr_{61}Cu_{39}$) with the respective error bars (shadowed regions), while the dash-dot lines refer to the ROM. The black dashed lines in (b,c) represent, respectively, the E and H values (as from literature[54]) for the Si (100) substrate.

physical origin of mechanical properties must consider a complex interconnection between substrate effects and mechanical size effects and that of the structural heterogeneities (interfaces/chemical intermixing) affecting the propagation of SBs.

Figure 2 shows that the presence of harder $Zr_{24}Cu_{76}$ layers and interfaces was able to hinder the percolation of SBs, inducing E and H values larger than the ROM even for 3 µm thick NLs. A similar effect is reported here for a total film thickness of 400 nm. Indeed, for Λ decreasing from 200 to 50 nm, the values of E and H gradually increase thanks to the SBs blocking effect gradually enhanced by the progressively larger number of interfaces, reaching exceptionally high values of E and H equal to 152 and 12.5 GPa (Figure 6b,c). This results from the presence of strong size effects triggered by the small total thickness (400 nm) as well as by the nanointerface confinement (with smaller bilayer period), creating a complex stress field during nanoindentation, affecting the propagation of SBs and leading to apparent high mechanical properties.[12,42] A further decrease of $\Lambda < 25$ nm leads to a drop of E and H, whose values are in line with the average of the NL constituents. This is due to the progressively less sharp interfaces and the formation of a more homogenous material, resulting in a less efficient barrier against SBs propagation.[17,43]

The cracking resistance of the amorphous NLs has been tested by tensile test on flexible Kapton substrates. The crack onset strain (COS) values for both 400 nm and 3 µm thick NLs as a function of Λ are reported in **Figure 7**a,b, respectively. In a previous study on monolithic ZrCu TFMGs,[24] we showed that $Zr_{24}Cu_{76}$ has a larger cracking resistance than $Zr_{61}Cu_{39}$ (up to 2%) due to the larger fraction of Cu–Cu bonds and the strong icosahedral atomic packing (Figure S7, SI). However, upon onset, the cracks immediately percolate through the entire sample (brittle behavior). For 400 nm thick NLs, the crack onset occurs at elongations close to that of monolithic $Zr_{61}Cu_{39}$ (i.e., $\approx 0.6\%$), therefore being affected by the presence in the stack of the weaker Zr-rich layers (Figure S7, SI). Nevertheless, the COS is influenced by the number of interfaces and it increases as Λ decreases, reaching a maximum of $\approx 1.2\%$ for $\Lambda = 40$ nm. A further decrement of Λ leads to a drop of COS down to $\approx 0.5\%$,

suggesting that the excessive increase in number of interfaces (i.e., free volume) promoted the crack nucleation tendency.

Interestingly, NLs show a crack-blocking effect as the onset of percolation occurs only at a later stage of deformation, as reported in the inset of Figure 7a for $\Lambda = 40$ nm, with COS $= 1.1\%$ and percolation threshold up to 2.9% (even considering the presence of $Zr_{61}Cu_{39}$ surface layer). The crack evolution images of the remaining 400 nm thick NLs are reported in Figure S8, SI. Glushko et al.[44] pointed out that during tensile test of TFMGs deposited on flexible substrates, SBs form both in the in-plane and out-of-plane directions with respect to the surface, but only the latter are responsible for formation of cracks. Therefore, the presence of heterogeneities and interfaces parallel to the film surface represents an obstacle to the propagation of out-of-plane SBs promoting crack-stopping effects within NLs, while mitigating the detrimental presence of weak Zr-rich layers and hindering their percolation. Similarly to the nanoindentation E and H trends, the COS increases when Λ decreases, reaching a maximum for $\Lambda = 40$ nm (Figure 7a). A further decrease of Λ leads to less sharp interfaces within the sublayers whose size is comparable to the SBs ones making the NLs heterogeneous structure less effective against SBs propagation (reduction of COS).

Figure 7b reports the COS for 3 µm thick films. First, it can be noticed that 3 µm thick monolithic films have a lower cracking resistance compared to their 400 nm thick counterparts (see Figure S9 and S10a,b, SI). The trend cannot be related to a difference in residual stress (ranging between 17 and 60 MPa) without showing any significant difference depending on the total thickness or on Λ (see Section S8 and Table S1, SI). Therefore, such difference can be attributed to the activation of mechanical size effects reporting an increase of cracking resistance for thinner films as a result of a reduced tendency of SBs formation.[45,46] Moreover, the 3 µm thick $Zr_{24}Cu_{76}$ does not show the crack-blocking ability of its thinner counterpart (COS equal to 1.2%) resulting in sharp cracks and immediate crack percolation after formation (see Figures S7a and S10a,b, SI).

However, the introduction of heterogeneities significantly affects the cracking behavior. In fact, the 3 µm thick NLs sustain
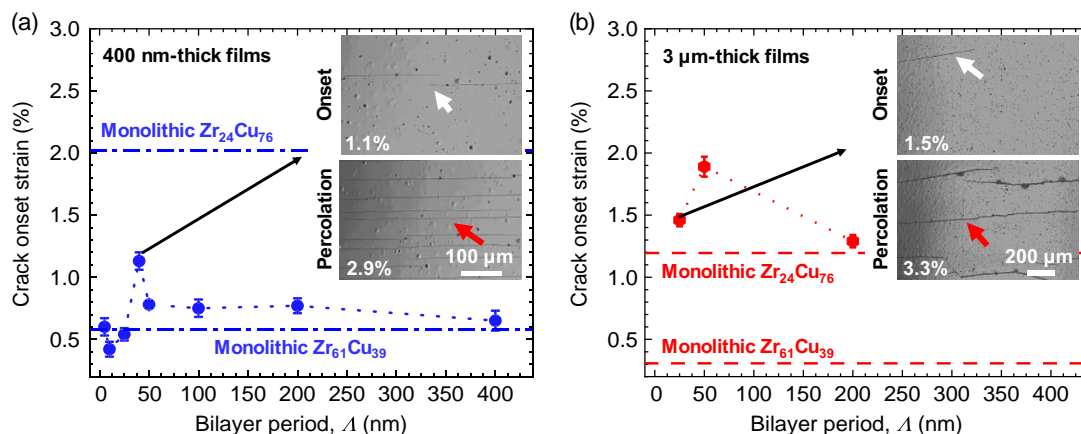
Figure 7. Cracking onset of NLs as a function of bilayer period (Λ) for a) 400 nm and b) 3 µm thick samples. In the insets, optical microscope images showing crack onset and percolation of NLs with (a) $\Lambda = 40$ nm and (b) $\Lambda = 25$ nm. Cracking onset values of NLs are compared to those of monolithic $Zr_{24}Cu_{76}$ and $Zr_{61}Cu_{39}$ with same total thickness.

higher cracking onsets than the 400 nm thick NLs (reaching the maximum of 1.9% for $\Lambda = 50$ nm), but also of the 3 μm thick monolithic counterparts (i.e., which have a COS of respectively of 0.3% and 1.2% for $Zr_{24}Cu_{76}$ and $Zr_{61}Cu_{39}$), as shown in Figure S9 and S10, SI. Similar to nanoindentation results, larger COS values for 3 μm thickness and high density of interfaces ($\Lambda = 50$ nm) are related to the size confinement within the NL structure and the higher number of interfaces, hindering crack nucleation and propagation. Moreover, similar to the 400 nm thick NLs, we show a tradeoff for the evolution of COS which initially increases as Λ is reduced from 200 down to 50 nm (increment in the number of interfaces) and then it decreases for $\Lambda = 25$ nm. This is due to the low layer thickness, providing more fertile sites for SBs nucleation and resulting as a macroscopically more homogenous material.[17,43]

More interestingly, we show that the 3 μm thick NLs exhibit a pronounced crack-deviation and crack-percolation resistance effects (insets in Figure 7b), indicating large ductility.[47] Specifically, the maximum values are obtained for $\Lambda = 50$ nm with an exceptional percolation onset of 3.3%. This value is far above expectations, even considering intrinsically more ductile $Pd_{82}Si_{18}$ TFMGs with total thickness of 16 nm (i.e. 3%) capable of triggering large mechanical size effects.[46] As a matter of fact, that for a fixed Λ, the 3 μm thick films have a larger number of interfaces and therefore an increased capability to interfere with the SBs propagation and their out-of-plane propagation. All these factors indicate that the increased presence of heterogeneities within the larger material volume (i.e., film thickness) enables to hinder the propagation of SBs and cracks, providing an easy way to tune the mechanical properties by controlling both their Λ and total thickness.

3. Conclusions

In this work, we develop a novel nanoengineering approach to tune heterogeneities within fully amorphous nanolaminates (NLs). We realize that in the form of easy-to-fabricate Zr_xCu_{100-x} NLs with controlled nanoscale periodicity and local chemistry. A large-scale-bridging structural/mechanical characterization enabled to investigate the deformation behavior, SBs nucleation/propagation, and the interaction with heterogeneities. We showed the following:

1) The heterogeneities can effectively stop the propagation of SBs, in correspondence of the layers with higher shear resistance. The path of SBs however induces a mismatch of the original NL configuration and a large chemical intermixing between the different layers. Nevertheless, layers resist to the passage of SBs, undergoing severe plastic deformations without dissolution;

2) A sufficiently high density of heterogeneities (i.e., bilayer period, $\Lambda = 50$ nm) enables larger elastic modulus and hardness, which can be further increased by reducing total thickness (i.e., 400 nm thick NLs), thanks to the activation of extrinsic confinement effects and substrate contribution reaching the ultimate values of 152 and 12.5 GPa, respectively;

3) Decreasing $\Lambda \leq 50$ nm leads to outstanding plasticity values > 15% in compression which can be reached due to the destructive interaction of multiple SBs and the presence

of shear resistance by Cu-rich regions, while keeping large yield strength > 1.6 GPa;

4) Extreme SBs/crack-blocking effects during tensile tests reported a large delay for their onset/percolation, reaching the ceiling values for 3 μm thick films with 1.8% (onset) and 3.3% (percolation) for $\Lambda = 25$ and 50 nm, respectively, significantly higher than the monolithic counterparts.

Overall, we show that the design of fully amorphous NL with controlled structural/chemical heterogeneities can opens a pathway for successfully application of such materials with improved/tunable mechanical properties in the field of micro and flexible electronics and of structural coatings.

4. Experimental Section

Synthesis of Fully Amorphous NLs: Magnetron sputtering was used for depositing ZrCu TFMGs, using different power ratios applied to the pure Cu and Zr targets to control film composition. Ar as a sputtering gas was introduced at 20 cm³ min⁻¹ with a chamber pressure of 0.5 Pa, while keeping the deposition temperature $T = T_{room}$ (more details reported in Ref. [24]). NLs were fabricated through an automatized deposition process, which alternatively changed the sputtering power and opened–closed both the substrate and cathodes shutters, controlling the thickness and composition of each layer. The two layer types always occupied the same volume fraction within the films: i.e., they had equal thickness and they were present in equal numbers. $Zr_{24}Cu_{76}$ was always the layer in contact with the substrate, while $Zr_{61}Cu_{39}$ was always at films' top surface. Films were deposited with both a thickness of 400 nm and 3 μm, while bilayer period (Λ) ranged from 400 down to 5 nm, on both Si (100) and Kapton substrates. Specifically, 400 nm thickness was selected to be compatible with optoacoustic measurements (see Section 2.3), while the 3 μm one was chosen for the milling of micropillars.

Structural Characterization: SEM (Zeiss-Gemini 500) was used to verify the films thickness and morphology, while the atomic structure and the interfaces of NLs were investigated by TEM. Several TEM cross-section lamella specimens were prepared by means of a Thermo Fisher Scios 2 dual-beam focus ion beam (FIB)–SEM from different nanoindented regions. SAED images were acquired with an C_s image-corrected Titan Themis 60–300 microscope (Thermo Fisher Scientific) at an acceleration voltage of 300 kV. STEM as well as EDS were performed on a spherical aberration (C_s) probe-corrected Titan Themis 60–300 operated at 300 kV equipped with the ChemiSTEM SuperX EDS detector system. The STEM investigations were done at a camera length of 100 mm, a semi-convergence angle of 23.5 mrad and a probe current of 90 pA.

EELS was carried at 300 kV at Thermo Fisher Titan with a 20 mrad convergence angle with a collection angle of 32.5 mrad for low-loss EELS measurement and a dispersion of 0.1 eV pixel⁻¹ and a pixel size of around 2 nm for the analysis of density of individual layers in NLs. For core loss, the collection angle was set to 65 mrad with a dispersion of 0.25 eV in dual-EELS mode. The low loss data was aligned on the zero loss peak and a Fourier-ratio deconvolution was used to determine the relative thickness.[48]

APT was used to investigate in-depth the chemical profile of NLs and the fluctuations within SBs. The APT specimen was prepared using the same dual-beam FIB–SEM as for TEM sample preparation. The APT sample fabrication protocols are described in Ref. [49]. The region deformed by the nanoindentation experiment was captured on the APT specimens. The APT analyses were performed using a local electrode atom probe (CAMECA LEAP 5000 XS) in a pulsed laser mode at a specimen base temperature of 50 K. A laser pulse energy of 40 pJ, a detection rate of 1%, and a laser pulse frequency of 125 kHz were used. Data reconstruction and analyses were carried out with the AP Suite 6.3 software (CAMECA Instruments).

Mechanical Characterization: The entire set of elastic constants was extracted by a combination of surface Brillouin spectroscopy (SBS) and

picosecond laser ultrasonic (PLU) optoacoustic technique. A complete description of optoacoustic SBS and PLU measurements can be found in the Section S9, Supporting Information, and in Refs. [24,50,51].

Nanoindentation measurements were performed in CSM configuration under load control with a load rate fixed to 0.05 s^{-1}, using a KLA G200 Nanoindenter DCM head equipped with a Berkovich tip and a similar experimental procedure as described in Ref. [24]. The values of hardness (H) and elastic modulus (E) were additionally extracted using the Oliver and Pharr method,[52] for depths below $\approx$10% of film thickness to avoid the influence of the Si (100) substrate.

The stress–strain curves were obtained by compression test of micropillars. Cylindrical micropillars were milled using an FIB within a Zeiss Auriga SEM. Milling was performed in three steps with currents ranging from 2 nA to 240 pA. The nominal diameter of the micropillars was fixed to a size of $\approx$1.2 μm, with an aspect ratio of $\approx$2.6 to suppress buckling instabilities and the taper angle was of $\approx$3°. For each sample, a total number of at least 5 pillars were tested. In situ SEM compression tests were conducted inside a Zeiss Gemini 500 SEM, using a Bruker Hysitron PI 88. All the tests were performed in pseudo-displacement-controlled mode at a nominal strain rate of 3×10^{-3} s^{-1}. To reduce the effect of lateral constraints, two unloading steps were performed during the compression tests, respectively at strains of $\approx$4% and $\approx$8% of strain to reduce the instrumental constraints.[53] Stress values were calculated using pillars top diameter surface area.

Film-cracking behavior was investigated by tensile tests on films deposited on flexible Kapton substrates, which were performed by imposing a tensile strain rate was of 1×10^{-4} s^{-1} and using the same setup and procedures described in Ref. [24]. The COS and the crack-percolation strains were identified corresponding to, respectively, the formation of the first visible cracks during deformation observed in the confocal microscope and the strain value in which the cracks cover the entire image. An objective with magnification of either 10x or 20x (i.e., with a corresponding image area of respectively 1570 × 1059 or 700 × 525 μm of size) was used to adequately observe cracks onset and propagation.

Supporting Information

Supporting Information is available from the Wiley Online Library or from the author.

Acknowledgements

Conflict of Interest

The authors declare no conflict of interest.

Data Availability Statement

The data that support the findings of this study are available from the corresponding author upon reasonable request.

[1] Z. Lei, X. Liu, Y. Wu, H. Wang, S. Jiang, S. Wang, X. Hui, Y. Wu, B. Gault, P. Kontis, D. Raabe, L. Gu, Q. Zhang, H. Chen, H. Wang, J. Liu, K. An, Q. Zeng, T.-G. Nieh, Z. Lu, *Nature* **2018**, *563*, 546.

[2] Z. Li, K. G. Pradeep, Y. Deng, D. Raabe, C. C. Tasan, *Nature* **2016**, *534*, 227.

[3] W. Klement, R. H. Willens, P. O. L. Duwez, *Nature* **1960**, *187*, 869.

[4] A. L. Greer, Y. Q. Cheng, E. Ma, *Mater. Sci. Eng.: R: Rep.* **2013**, *74*, 71.

[5] W. L. Johnson, K. Samwer, *Phys. Rev. Lett.* **2005**, *95*, 195501.

[6] K. Nomoto, A. V. Ceguerra, C. Gammer, B. Li, H. Bilal, A. Hohenwarter, B. Gludovatz, J. Eckert, S. P. Ringer, J. J. Kruzic, *Mater. Today* **2021**, *44*, 48.

[7] K. Nomoto, B. Li, C. Gammer, A. V. Ceguerra, H. Bilal, A. Hohenwarter, J. Eckert, B. Gludovatz, S. P. Ringer, J. J. Kruzic, *Phys. Rev. Mater.* **2022**, *6*, 043603.

[8] H. Idrissi, M. Ghidelli, A. Béché, S. Turner, S. Gravier, J.-J. Blandin, J.-P. Raskin, D. Schryvers, T. Pardoen, *Sci. Rep.* **2019**, *9*, 13426.

[9] W. Li, H. Bei, Y. Tong, W. Dmowski, Y. F. Gao, *Appl. Phys. Lett.* **2013**, *103*, 171910.

[10] Y. Ivanisenko, C. Kübel, S. H. Nandam, C. Wang, X. Mu, O. Adjaoud, K. Albe, H. Hahn, *Adv. Eng. Mater.* **2018**, *20*, 1800404.

[11] M. Ghidelli, A. Orekhov, A. L. Bassi, G. Terraneo, P. Djemia, G. Abadias, M. Nord, A. Béché, N. Gauquelin, J. Verbeeck, J. P. Raskin, D. Schryvers, T. Pardoen, H. Idrissi, *Acta Mater.* **2021**, *213*, 116955.

[12] M. Ghidelli, S. Gravier, J. J. Blandin, P. Djemia, F. Mompiou, G. Abadias, J. P. Raskin, T. Pardoen, *Acta Mater.* **2015**, *90*, 232.

[13] M. Ghidelli, H. Idrissi, S. Gravier, J.-J. Blandin, J.-P. Raskin, D. Schryvers, T. Pardoen, *Acta Mater.* **2017**, *131*, 246.

[14] J.-Y. Kim, D. Jang, J. R. Greer, *Adv. Funct. Mater.* **2011**, *21*, 4550.

[15] W. Guo, E. Jägle, J. Yao, V. Maier, S. Korte-Kerzel, J. M. Schneider, D. Raabe, *Acta Mater.* **2014**, *80*, 94.

[16] Z. Q. Chen, M. C. Li, J. S. Cao, F. C. Li, S. W. Guo, B. A. Sun, H. B. Ke, W. H. Wang, *J. Mater. Sci. Technol.* **2022**, *99*, 178.

[17] S. Y. Kuan, H. S. Chou, M. C. Liu, X. H. Du, J. C. Huang, *Intermetallics* **2010**, *18*, 2453.

[18] P. Sharma, K. Yubuta, H. Kimura, A. Inoue, *Phys. Rev. B* **2009**, *80*, 024106.

[19] G. Wu, C. Liu, A. Brognara, M. Ghidelli, Y. Bao, S. Liu, X. Wu, W. Xia, H. Zhao, J. Rao, D. Ponge, V. Devulapalli, W. Lu, G. Dehm, D. Raabe, Z. Li, *Mater. Today* **2021**, *51*, 6.

[20] M. Y. Tong, C. K. C. Lieou, I. J. Beyerlein, *Phys. Rev. Mater.* **2019**, *3*, 073602.

[21] P. Kontis, M. Köhler, S. Evertz, Y. T. Chen, V. Schnabel, R. Soler, J. Bednarick, C. Kirchlechner, G. Dehm, D. Raabe, J. M. Schneider, B. Gault, *Scr. Mater.* **2018**, *155*, 73.

[22] G. Wu, S. Liu, Q. Wang, J. Rao, W. Xia, Y.-Q. Yan, J. Eckert, C. Liu, E. Ma, Z.-W. Shan, *Nat. Commun.* **2023**, *14*, 3670.

[23] Y. Zhang, A. L. Greer, *Appl. Phys. Lett.* **2006**, *89*, 071907.

[24] A. Brognara, J. P. Best, P. Djemia, D. Faurie, G. Dehm, M. Ghidelli, *Mater. Des.* **2022**, *219*, 110752.

[25] H. Aboulfadl, F. Seifried, M. Stüber, F. Mücklich, *Mater. Lett.* **2019**, *236*, 92.

[26] Y. Q. Cheng, A. J. Cao, H. W. Sheng, E. Ma, *Acta Mater.* **2008**, *56*, 5263.

[27] Y. J. Li, P. Choi, C. Borchers, S. Westerkamp, S. Goto, D. Raabe, R. Kirchheim, *Acta Mater.* **2011**, *59*, 3965.

[28] P. Y. Tung, X. Zhou, D. Mayweg, L. Morsdorf, M. Herbig, *Acta Mater.* **2021**, *216*, 117144.

[29] D. Pan, A. Inoue, T. Sakurai, M. W. Chen, *Proc. Natl. Acad. Sci.* **2008**, *105*, 14769.

[30] S. Balachandran, J. Orava, M. Köhler, A. J. Breen, I. Kaban, D. Raabe, M. Herbig, *Scr. Mater.* **2019**, *168*, 14.

[31] K. S. Nakayama, Y. Yokoyama, G. Xie, Q. S. Zhang, M. W. Chen, T. Sakurai, A. Inoue, *Nano Lett.* **2008**, *8*, 516.

[32] J. J. Lewandowski, A. L. Greer, *Nat. Mater.* **2006**, *5*, 15.

[33] V. Z. Bengus, E. D. Tabachnikova, J. Miškuf, K. Csach, V. Ocelík, W. L. Johnson, V. V. Molokanov, *J. Mater. Sci.* **2000**, *35*, 4449.

[34] M. C. Liu, J. C. Huang, H. S. Chou, Y. H. Lai, C. J. Lee, T. G. Nieh, *Scr. Mater.* **2009**, *61*, 840.

[35] A. Bharathula, S.-W. Lee, W. J. Wright, K. M. Flores, *Acta Mater.* **2010**, *58*, 5789.

[36] Y. Q. Cheng, H. W. Sheng, E. Ma, *Phys. Rev. B* **2008**, *78*, 014207.

[37] S. H. Nandam, Y. Ivanisenko, R. Schwaiger, Z. Śniadecki, X. Mu, D. Wang, R. Chellali, T. Boll, A. Kilmametov, T. Bergfeldt, H. Gleiter, H. Hahn, *Acta Mater.* **2017**, *136*, 181.

[38] J. X. Fang, U. Vainio, W. Puff, R. Würschum, X. L. Wang, D. Wang, M. Ghafari, F. Jiang, J. Sun, H. Hahn, H. Gleiter, *Nano Lett.* **2012**, *12*, 458.

[39] Z. Han, W. F. Wu, Y. Li, Y. J. Wei, H. J. Gao, *Acta Mater.* **2009**, *57*, 1367.

[40] S. H. Nandam, R. Schwaiger, A. Kobler, C. Kübel, C. Wang, Y. Ivanisenko, H. Hahn, *J. Mater. Res.* **2021**, *36*, 2903.

[41] C. Rossignol, B. Perrin, B. Bonello, P. Djemia, P. Moch, H. Hurdequint, *Phys. Rev. B* **2004**, *70*, 094102.

[42] J. R. Greer, J. T. M. De Hosson, *Prog. Mater. Sci.* **2011**, *56*, 654.

[43] K. Madani, M. Belhouari, B. Bachir Bouiadjra, B. Serier, M. Benguediab, *Comput. Mater. Sci.* **2007**, *38*, 625.

[44] O. Glushko, C. Gammer, L.-M. Weniger, H. Sheng, C. Mitterer, J. Eckert, *Mater. Today Commun.* **2021**, *28*, 102547.

[45] K. Wu, Y. Q. Wang, H. Z. Yuan, J. Y. Zhang, G. Liu, J. Sun, *Philos. Mag. Lett.* **2018**, *98*, 464.

[46] O. Glushko, M. Mühlbacher, C. Gammer, M. J. Cordill, C. Mitterer, J. Eckert, *Sci. Rep.* **2019**, *9*, 8281.

[47] C. H. Li, R. Dedoncker, L. W. Li, F. Sedghgooya, F. Zighem, V. Ji, D. Depla, P. Djemia, D. Faurie, *Surf. Coat. Technol.* **2020**, *402*, 126474.

[48] T. Malis, S. C. Cheng, R. F. Egerton, *J. Electron Microsc. Tech.* **1988**, *8*, 193.

[49] K. Thompson, D. Lawrence, D. J. Larson, J. D. Olson, T. F. Kelly, B. Gorman, *Ultramicroscopy* **2007**, *107*, 131.

[50] P. Djemia, A. Fillon, G. Abadias, A. Michel, C. Jaouen, *Surf. Coat. Technol.* **2011**, *206*, 1824.

[51] F. Xu, L. Belliard, D. Fournier, E. Charron, J. Y. Duquesne, S. Martin, C. Secouard, B. Perrin, *Thin Solid Films* **2013**, *548*, 366.

[52] W. C. Oliver, G. M. Pharr, *J. Mater. Res.* **2011**, *19*, 3.

[53] D. Kiener, C. Motz, G. Dehm, *Mater. Sci. Eng., A* **2009**, *505*, 79.

[54] Y.-G. Jung, B. R. Lawn, M. Martyniuk, H. Huang, X. Z. Hu, *J. Mater. Res.* **2004**, *19*, 3076.